Numerical Studies of Motion and Decay of Vortex Filaments

C. H. Liu*
NASA Langley Research Center, Hampton, Virginia
John Tavantzis†
New Jersey Institute of Technology, Newark, New Jersey
and
Lu Ting‡
New York University, New York, New York

A computational code is developed for the integro-differential equations governing the motion of the centerlines of vortex filaments submerged in a background potential flow. These equations, which are derived from the method of matched asymptotic analysis, include the effect of decaying large-magnitude circumferential and axial velocity components in the vortical cores. Numerical examples are presented to assess the effect of large axial velocity and of nonsimilar initial profiles in vortical cores. The initial configurations of the filaments are chosen so as to fulfill the basic assumption of asymptotic analysis, which is the effective vortical core size is much smaller than all other length scales in the flowfield, e.g., the radius of curvature and interfilament distance. The computations are continued until the basic assumption is no longer valid, that is, when the merging or intersection of filaments have begun. Various types of local or global merging or intersection of filaments are classified and demonstrated by numerical examples.

I. Introduction

IN flows around wings, propellers, and bodies[1-3] and in many natural aerodynamics problems,[4-6] effects of vorticity are important. In these flowfields, the bulk of vorticity is usually concentrated in slender "tubelike" regions called vortex filaments. The size of the cross section of a filament is small compared to other length scales characterizing the flowfield. Away from these regions, the flow can be considered as irrotational.

In the classical inviscid theory, the cross-sectional area of the tube is reduced to zero and the slender tubelike filament becomes a vortex line. The velocity $\boldsymbol{Q}_1(\boldsymbol{P},t)$ at point P induced by the vortex line C is defined by the Biot-Savart integral along the vortex line (see Ref. 7),

$$\boldsymbol{Q}_1(\boldsymbol{P},t)=\frac{\Gamma}{4\pi}\int_C \frac{\boldsymbol{X}'-\boldsymbol{P}}{|\boldsymbol{X}'-\boldsymbol{P}|^3}\times d\boldsymbol{X}' \tag{1}$$

where Γ is the circulation around the vortex line C. The position vector of the point P and of a point on the vortex line are denoted by $\boldsymbol{P}$ and $\boldsymbol{X}'$, respectively. Near the vortex line, $r=|\boldsymbol{P}-\boldsymbol{X}|\to 0$, the velocity $\boldsymbol{Q}$ behaves as

$$\boldsymbol{Q}_1=\frac{\Gamma}{2\pi r}\hat{\theta}+\frac{\Gamma}{4\pi R}\ell n\left(\frac{\delta}{r}\right)\hat{b}+\frac{\Gamma\cos\phi}{4\pi R}\hat{\theta}+\boldsymbol{Q}_f \tag{2}$$

where $\boldsymbol{X}$ denotes the point on C nearest to P. In Eq. (2), $\hat{\theta}$, $\hat{b}$, and R are the unit circumferential vector, the binormal vector, and the radius of curvature of C at X, respectively, and ϕ denotes the angle between the unit normal vector $\hat{n}$ of C at X and the radial vector $\boldsymbol{P}-\boldsymbol{X}$ (see Fig. 1). The first three terms on the right side of Eq. (2) are the singular parts, and the last term $\boldsymbol{Q}_f$, is the finite part of $\boldsymbol{Q}$, i.e., $\boldsymbol{Q}_f$ has a limit as $r\to 0$. A length scale δ is introduced in Eq. (2) to nondimensionalize the argument of the logarithmic term. Its contribution will be canceled by a $\ell n\delta$ term in $\boldsymbol{Q}_f(\boldsymbol{X},t)$ and hence will not affect $\boldsymbol{Q}_1$. The length δ is identified in the asymptotic analysis as the effective core size so that $r/\delta=O(1)$ in the "inner" region.

From Eq. (2), it is evident that the classical theory suffers from two serious defects: 1) the fluid velocity on the vortex line becomes infinite, and 2) the velocity of the vortex line itself is undefined. In a real fluid the velocity field and its gradient must remain finite everywhere. In the inner region where the velocity and hence the gradient of the velocity become large, the viscous terms become the mechanism by which the velocity gradients are attenuated. The defects of classical inviscid theory for vortex motion can therefore be eliminated if the inviscid solution is identified as the leading term of a matched asymptotic solution of the incompressible Navier-Stokes equations in a region (the outer region) sufficiently far away from the filament. The viscous terms become important in the inner region. The condition that the velocity should be finite everywhere then enables us to define the velocity of a filament with a large vorticity distribution in the core structure. With this premise, the matched asymptotic solution for a vortex filament submerged in an outer potential flowfield was constructed in a series of four papers[8-11] starting from two-dimensional problems for vortices[8] to three-dimensional problems in which both circumferential and axial velocity components in the vortical core[11] are large. The small parameter in the asymptotic expansion is

$$\epsilon=\sqrt{\nu/\Gamma}=(\text{Reynolds number})^{-1/2}\ll 1 \tag{3}$$

where ν is the kinematic viscosity and Γ is the circulation around the filament. The effective core size δ is assumed to be of order ϵ compared with the reference length L of all

Received July 8, 1985; revision received Dec. 23, 1985.

*Leader, Vortex Flow Analysis Group, Analytical Methods Branch. Senior Member AIAA.
†Associate Professor of Mathematics.
‡Professor of Mathematics, Courant Institute of Mathematical Sciences. Member AIAA.

other length scales in the flowfield, i.e.,

$$\delta/L = O(\epsilon) \ll 1 \tag{4}$$

The asymptotic analysis[11] enables us to reduce the unsteady three-dimensional Navier-Stokes equations to a system of integro-differential equations in time t and one spatial variable s for the motion of the centerlines of the vortex filaments. These equations contain terms representing the bulk effects of the inner structures, that is, the large axial vorticity ζ (or the circumferential velocity v) and the axial velocity w. The leading governing equations for the diffusion of the inner structures are reduced to two simple heat-conduction equations by appropriate transformation of variables involving the length of the filament to account for the stretching effect on the core size. Analytical solutions for the core structures and the expressions for their bulk contributions to the integro-differential equations for the motion of the filaments are then obtained. These expressions and the integro-differential equations form a closed system.

The essential results of the asymptotic analysis of Ref. 11, with some minor corrections and modifications, are summarized in Sec. II. The computational code for the motion and decay of the vortex filaments are then developed.

In Sec. III, numerical examples are presented to show the effects of large-magnitude axial flow and nonsimilar initial core structure on the motion of the filaments. Examples are selected to illustrate when and where the asymptotic analysis ceases to be valid as merging or intersection of vortex filaments takes place in violation of condition (4).

In Sec. IV, various types of merging of vortex filaments are illustrated by numerical examples and classified into three types. For each type, a finite domain D containing the merged region can be selected so that numerical solutions of the Navier-Stokes equations in D can be constructed to study their merging.

It should be pointed out that beside the matched asymptotic analyses[8-11] mentioned above, there are other vortex methods based on inviscid theory with artificial smoothing[12-18] and/or patching[19-21] to remove the singularity in the Biot-Savart formula for the self-induced velocity. In order to emphasize the differences between these inviscid solutions and our viscous solutions, we summarize some key features of our matched asymptotic analysis.[11] They are:

1) The large (order ϵ^{-1}) axial velocity w and circumferential velocity v in the core of a filament are functionally related. (This dependence holds also for inviscid theory). In particular, if v is independent of the parameter s along the filament, so is w. The converse is also true. When there is no large axial flow, the large circumferential velocity v has to be independent of s. Consequently, the core size and the stretching effect on the vorticity distribution must be uniform along the filament and must depend only on its length $S(t)$.

2) The vortical core structure—in particular, its effective size—appears in the dominant term of the velocity of a vortex filament. The variation of the core size due to stretching and diffusion is properly accounted for in the asymptotic solution. The diffusion effect becomes more important as the core size decreases due to stretching.

3) The self-induced velocity of the vortex filament also contains the finite part of the Biot-Savart integral. The finite part is obtained[11] by canceling analytically the singular parts, so that the resulting integrand of the finite part is piecewise continuous. The finite part having piecewise continuous integrand can be evaluated numerically. It depends not only on the local curvature but also on the local torsion and the derivative along the centerline.

We now compare these properties with those in the inviscid solutions.[12-21] The first three references[12-14] treat the dynamics of two-dimensional inviscid vortices. We note the correspondence with two-dimensional asymptotic analysis in that the leading velocity of a vortex center agrees with that of the inviscid theory and is independent of the viscous core structure as long as the vortices are far apart relative to their core sizes.

The three-dimensional inviscid vortex methods are presented in Refs. 15-18, where the singularity in the Biot-Savart integral is artificially smoothed. For example, in Refs. 15-17, the denominator $|X'-P|^3$ in Eq. (1) is replaced by $h^2|X'-P|$ when $|X'-P|<h$, where h is a preassigned small value. On the other hand, in Ref. 18 the singularity is removed when $|X'-P|$ is replaced by $\{|X'-P|^2+\delta_i^2+\delta_j^2\}^{1/2}$, where X' and P are points on the ith and jth vortex lines and δ_i and δ_j are the corresponding core size. Thus, the velocity on a vortex line is rendered finite. The vortex line is then treated as a material line, and the local stretching of the line in turn defines the variation of the core size.[15] Hence, the core size is not uniform[15,18] along a vortex line in contrast to preceding feature 1 of the asymptotic solution. We note that the motion of a curve is defined by its normal and binormal velocity components and is independent of the tangential component. The tangential velocity of an inviscid vortex line of finite strength Γ is the outer limit (where the vorticity vanishes) of the axial velocity of the inner region. The convection of the vorticity distribution in the core is defined by the velocity in the inner region and is properly accounted for in the matched asymptotic solution,[10,11] which in addition includes the viscous diffusion effect. This explains the discrepancies between their inviscid solutions and our asymptotic solution.

There is another vortex method based on the inviscid theory patched with a diffusive inner core modeled by a similarity solution. The latter is Lamb's solution[7] for the decay of an isolated straight filament.[19,20] A computational code based on the equations for the patched solutions with the variation of the core size related to the length of the filament was developed by Leonard.[21] The equations of this code are consistent with the aforementioned feature 1, subject to the restriction that in the core there is a large similar circumferential flow but no large axial flow. Furthermore, the evaluation of the finite part is obtained by approximating the local arc of the filament by a circular one. These differ from features 2 and 3 of our solution.

II. Equations of Motion for the Vortex Filaments

Let us consider the flowfield of N vortex filaments in a background flow with velocity potential $\Phi(X)$. Let Γ_i and $X_i(s_i,t)$ denote the circulation and position vector of the centerline of the ith filament, for $i=1,2,\ldots,N$. The parameter s_i increases in the direction of positive Γ_i. The subscript i will be suppressed from here on. For each filament, the initial centerline C and its inner structure, i.e., the large axial and circumferential velocity distribution, are prescribed. They should be consistent with conditions 3 and 4 of the asymptotic analysis. The equation for the velocity of the ith filament X_t is[11]

$$X_t(s,t) = Q^*(X,t) + \frac{\Gamma}{4\pi R}\left[\ell n\,\frac{R}{\delta(t)} + C_v(t)\right]\hat{b} + \frac{C_w(t)}{4\pi R}\,\hat{b} \tag{5}$$

where $Q^* = Q_2 + Q_f - \hat{\tau}[(Q_2+Q_f)\cdot\hat{\tau}]$. The removal of the tangential component of Q_2 and Q_f insures that $\hat{\tau}\cdot X_t = 0$. Here $Q_2(X,t)$ denotes the velocity of the flowfield at X in the absence of the ith filament,

$$Q_2 = \nabla\Phi(X) + \frac{1}{4\pi}\sum_{\substack{j=1\\ j\neq i}}^{N}\Gamma_j\int_{C_j}\frac{X_j - X}{|X_j - X|^3}\times dX_j \tag{6}$$

and $Q_f(s,t)$ is the finite part of the Biot-Savart integral, defined in Eqs. (1) and (2) for the ith filament at X. In the

matched asymptotic analysis,[11] the singular parts in Eq. (2) are canceled analytically and the finite part $\boldsymbol{Q}_f$ is given by

$$\boldsymbol{Q}_f(s,t)=\frac{\Gamma}{4\pi}\left\{\int_{-\pi}^{\pi}\boldsymbol{H}(s+\bar{s},s,t)\mathrm{d}\bar{s}+\left[\ell_n\frac{2\sqrt{S_+S_-}}{R}-1\right]\frac{\hat{b}}{R}\right\} \tag{7}$$

where

$$\boldsymbol{H}(s',s,t)=\boldsymbol{F}(s',s,t)-2\hat{b}/(R|\lambda|) \qquad \text{for } s'\neq s \tag{8a}$$

$$=\hat{\tau}\times\boldsymbol{B}\,\mathrm{sgn}(s'-s)/3 \qquad \text{for } s'=s^{\pm} \tag{8b}$$

$$\boldsymbol{F}(s',s,t)=\frac{\boldsymbol{X}(s',t)-\boldsymbol{X}(s,t)}{|\boldsymbol{X}(s',t)-\boldsymbol{X}(s,t)|^3}\times\boldsymbol{X}_s(s,t) \qquad \text{for } s'\neq s \tag{8c}$$

with

$$\sigma(s,t)=|\boldsymbol{X}_s(s,t)| \tag{9a}$$

$$\lambda(s',s,t)=\int_s^{s'}|\sigma(s^*,t)|\mathrm{d}s^* \tag{9b}$$

$$\boldsymbol{B}(s,t)=\frac{-\sigma\hat{\tau}}{R^2}+\frac{\partial}{\partial s}\left(\frac{1}{R}\right)\hat{n}+\frac{T}{R}\sigma\hat{b} \tag{9c}$$

$$S_{\pm}=\lambda(s\pm\pi,s,t) \tag{9d}$$

We denote the unit tangent, normal and binormal vectors, and the radius of curvature and torsion of the centerline by $\hat{\tau}$, $\hat{n}$, $\hat{b}$, R, and T, respectively. They are related to $\boldsymbol{X}(s,t)$ by the Serret-Frenet formulas,

$$\boldsymbol{X}_s=\sigma\hat{\tau}, \qquad \boldsymbol{X}_s\times\boldsymbol{X}_{ss}=\sigma^3\hat{b}/R,$$

$$\hat{b}\times\hat{\tau}=\hat{n}, \qquad T=\frac{-1}{\sigma}\frac{\partial\hat{b}}{\partial s}\cdot\hat{n} \tag{10}$$

Without loss of generality, the parameter s has been so chosen that $\boldsymbol{X}(s,t)$ is initially periodic in s with period 2π and hence for all t. The length of the centerline is

$$S(t)=S_+(t)+S_-(t)=\int_0^{2\pi}|\sigma(s,t)|\mathrm{d}s \tag{11}$$

Note that the integrand $\boldsymbol{H}$ in Eq. (7) is a piecewise continuous function of $\bar{s}=s'-s$, with the jump discontinuity at $\bar{s}=0$ defined in Eq. (8b). Therefore $\boldsymbol{Q}_f$ given by Eq. (7) can be evaluated numerically at each instant. We remark that Eqs. (5-11) substantiate features 2 and 3 stated in the Introduction.

The remaining three unknowns, $\delta(t)$, $C_v(t)$, and $C_w(t)$, are related to the inner structures of the filament. In the analysis of the inner region, the spacial variables in the Cartesian coordinates are transformed to the toroidal coordinates. They are the parameter s for the centerline, local radial variable r, the circumferential variable θ (see Fig. 1 and Refs. 10 and 11). The radial variable is then stretched by the factor ϵ^{-1}, i.e.,

$$\bar{r}=r/\epsilon \tag{12}$$

The analysis then shows that the large circumferential and axial velocity v and w are of order ϵ^{-1} and that their leading terms are independent of θ. Furthermore, if either one of them is independent of s, so is the other. We therefore express the velocity in the inner region as

$$u=O(1), \qquad v=\epsilon^{-1}\bar{v}(\bar{r},t)+O(1), \qquad w=\epsilon^{-1}\bar{w}(\bar{r},t)+O(1) \tag{13}$$

Again we remark that Eq. (13) is feature 1.

The initial data for $\bar{v}$ and $\bar{w}$ should be functions of $\bar{r}$ only, i.e., $\bar{v}(\bar{r},0)=\bar{v}_0(\bar{r})$ and $\bar{w}(\bar{r},0)=\bar{w}_0(\bar{r})$. The leading circumferential velocity $\epsilon^{-1}\bar{v}$ is related to the leading axial vorticity $\epsilon^{-2}\bar{\zeta}(\bar{r},t)$ by the equation

$$\bar{v}=\frac{1}{\bar{r}}\int_0^{\bar{r}}\bar{r}'\bar{\zeta}\mathrm{d}\bar{r}' \tag{14}$$

We can specify either the initial data for $\bar{v}$ or for $\bar{\zeta}$. Also, note that the total strength of ζ is the time-invariant circulation Γ,

$$\Gamma=2\pi\int_0^{\infty}\bar{\zeta}(\bar{r},t)\bar{r}\mathrm{d}\bar{r}=2\pi\int_0^{\infty}\bar{\zeta}_0(\bar{r})\bar{r}\mathrm{d}\bar{r} \tag{15}$$

The solutions for the leading inner structures were obtained[11] in a series of Laguerre polynomials L_n. They are

$$\bar{\zeta}(\bar{r},t)=S(t)e^{-\eta^2}\sum_{n=0}^{\infty}D_nL_n(\eta^2)\tau_1^{-(n+1)} \tag{16a}$$

$$\bar{w}(\bar{r},t)=\frac{1}{S(t)}e^{-\eta^2}\sum_{n=0}^{\infty}C_nL_n(\eta^2)\tau_1^{-(n+1)} \tag{16b}$$

$$\bar{v}(\bar{r},t)=\frac{2\Gamma}{\bar{r}}\left\{D_0(1-e^{-\eta^2})+e^{-\eta^2}\sum_{1}^{\infty}D_n[L_{n-1}(\eta^2)-L_n(\eta^2)]/\tau_1^n\right\} \tag{16c}$$

Here τ_1 and η are two new variables replacing t and $\bar{r}$ with

$$\dot{\tau}_1=S(t) \text{ or } \tau_1=\int_0^t S(t')\mathrm{d}t'+\tau_{10} \tag{17}$$

$$\eta=\bar{r}/(4\Gamma\tau_1/S)^{1/2}=r/\delta(t) \tag{18a}$$

$$\delta(t)=[4\nu\tau_1(t)/S(t)]^{1/2} \tag{18b}$$

Since $\bar{\zeta}$, $\bar{w}$, and $\bar{v}$ in Eqs. (16a-16c) have a decaying factor $\exp(-\eta^2)$, which becomes $1/e$ when $\eta=1$ or $r=\delta$, we identify $\delta(t)$ as the effective core size.

The constants C_n and D_n in Eq. (16) are determined in terms of the initial values of $\bar{\zeta}$ and $\bar{w}$,

$$C_n=2S_0\left(\frac{\tau_{20}}{S_0}\right)^{n+1}\int_0^{\infty}\bar{w}_0(\bar{r})L_n(\eta^2)\eta\mathrm{d}\eta \tag{19a}$$

$$D_n=\frac{2}{S_0}\left(\frac{\tau_{20}}{S_0}\right)^{n+1}\int_0^{\infty}\bar{\zeta}_0(\bar{r})L_n(\eta^2)\eta\mathrm{d}\eta \tag{19b}$$

where $\bar{r}=\eta(4\Gamma\tau_{20})^{1/2}$, $S_0=S(0)$, $\tau_{20}=\tau_{10}/S_0$, $\delta_0=(4\nu\tau_{10}\div S_0)^{1/2}$. Here S_0 and δ_0 are the initial length and effective core size.

We note that for

$$n=0, \quad C_0=M_0/(4\Gamma\pi\epsilon),$$

$$D_0=1/(\pi S_0^2), \text{ and } M_0=2\pi\int_0^{\infty}(\epsilon^{-1}\bar{w}_0)(\epsilon^2\bar{r}\mathrm{d}\bar{r})$$

The quantity M_0 is the initial axial mass flux. When C_n and D_n vanish for $n \geq 1$, $\bar{v}$ and $\bar{w}$ are represented by the first term in Eqs. (16a) and (16b), respectively. They are the similarity solutions defined by the total axial vorticity Γ, the initial axial momentum M_0, and the initial core size δ_0.

In Eqs. (17) and (18), δ_0 is defined by an arbitrary positive constant τ_{10}. An optimum τ_{10} is defined by the condition $D_1 = 0$ so that the first term in Eq. (16a) becomes the dominant term in the shortest time and is called the optimum similarity solution.[10] The condition for optimum τ_{10} is

$$\int_0^\infty \bar{\zeta}_0(\bar{r})[1-\eta^2]\eta \mathrm{d}\eta = 0 \quad \text{or} \quad \tau_{10} = \frac{\pi}{2\Gamma^2} S_0 \int_0^\infty \bar{\zeta}\bar{r}^3 \mathrm{d}\bar{r} \quad (20)$$

Thus, the first term in Eq. (16a) preserves not only the total strength but also the second polar moment of the initial vorticity distribution $\bar{\zeta}_0$.

The remaining two unknowns C_v and C_w in Eq. (5) are related to the inner structures of $\bar{v}(\bar{r},t)$ and $\bar{w}(\bar{r},t)$[11]

$$C_v(t) = \lim_{\bar{r}\to\infty} \left\{ \frac{4\pi^2}{\Gamma^2} \int_0^{\bar{r}} \xi[\bar{v}(\xi,t)]^2 \mathrm{d}\xi - \ell n \frac{\bar{r}}{\sqrt{4\Gamma\tau_2}} \right\} + \frac{1}{2} \quad (21a)$$

$$C_w(t) = -\frac{8\pi^2}{\Gamma} \int_0^\infty \xi[\bar{w}(\xi,t)]^2 \mathrm{d}\xi \quad (21b)$$

These improper integrals have been evaluated analytically and found to be

$$C_v(t) = \frac{1}{2}\{1+\gamma-\ell n 2\} + 4\pi \sum_{n=1}^{N} \alpha_n \tau_1^{-n}(t) + 8\pi \sum_{n=2}^{N} \gamma_n \tau_1^{-n}(t) \quad (22a)$$

with

$$\alpha_n = D_n \sum_{j=1}^{N} q_{n,j}[(j-1)!]\{1-2^{-j}\}$$

$$\gamma_h = \sum_{m=1}^{h} D_m D_{h-m} \beta_{m,h-m'}$$

$$\beta_{n,h} = \sum_{i=1}^{n} (p_{n-1,i} - p_{n,i}) \sum_{j=1}^{h} (p_{h-1,j} - p_{h,j})(i+j-1)!/2^{i+j}$$

$$C_w = -\frac{16\pi^2}{S^3(t)\tau_1(t)} \sum_{n=0}^{N} \tau_1^{-n}(t)\omega_n \quad (22b)$$

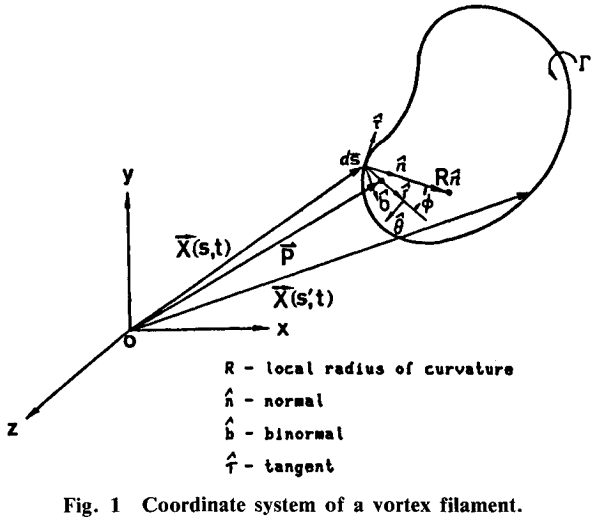

Fig. 1 Coordinate system of a vortex filament.

with

$$\omega_n = \sum_{m=0}^{n} C_m C_{n-m} P_{m,n-m'}, \quad P_{n,i} = \sum_{j=0}^{i} p_{i,j} \sum_{k=0}^{n} p_{n,k}(j+k)!/2^{j+k+1}$$

Here γ is the Euler number, $(N+1)$ is the number of terms used in the series representations (16) of $\bar{v}$ and $\bar{w}$ to fit the initial data, and $p_{n,k}$ is the coefficient of x^k in the Leguerre polynomial $L_n(x)$. For similar inner structures, i.e., $C_n = 0$, $D_n = 0$ for $n \geq 1$, C_v and C_w are defined by the first term on the right side of Eqs. (22a) and (22b), respectively.

Thus, for a given initial core structure, Eqs. (19a), (19b), and (20) define the constants C_n, D_n, and τ_{10}, which in turn define the initial effective core size $\delta(0)$ by Eq. (18).

Equations (5) and (17) can be considered to be the evolution equations for the centerline $X(s,t)$ and the time scale $\tau_1(t)$. The latter provides the coupling between the effective core size δ and the length of the filament S by Eqs. (18) and (11). Equations (9-11) define the relevant geometric properties of the centerline $X(s,t)$ while Eqs. (6-8) and (22) define the right-hand side of Eq. (5), i.e., the background local velocity $\boldsymbol{Q}_2$, the finite part of the self-induced velocity $\boldsymbol{Q}_f$, and the bulk contributions of the inner structure C_v and C_w.

Equations (5) and (17), supplemented by Eqs. (6-11), (18), and (22) applied to the ith filament for $i = 1,\ldots,N$, for a closed system of equations of motion for the N filaments when the initial configurations for the centerlines $X_i(s_i,0)$ and their initial inner structures are specified.

Linear stability analyses for several finite-difference schemes were carried out[22] for the limiting case of very large $\ell n(1/\epsilon)$. The dominant term of the velocity X_t, Eq. (5), will then be $[\Gamma/(4\pi R)]\ell n(1/\epsilon)$, which contains only the effect of local curvature with a constant core size and is uncoupled from the background flow and from the global properties of the filament. It was shown in the Appendix of Ref. 22 that 1) the standard explicit scheme is always unstable, 2) the DuFort-Frankel scheme can be modified so that it becomes stable, and 3) the implicit scheme is always stable.

In our computational code for the full system of integro-differential equations, the implicit scheme is used. We first pick the numbers of grid points J_i on the ith filament with ΔS_i equal to $2\pi/J_i$ for $i = 1,\ldots,N$. We choose the first step Δt such that the Courant-Friedrich-Levy (CFL) number is less than an assigned value smaller than unity. We use the maximum velocity of the jth grid point and the minimum segment length $|X_{j,i} - X_{j-1,i}|$ for $j = 1,\ldots,J_i$ (MOD J_i) and $i = 1,\ldots,N$ as the reference velocity and segment length in CFL number. For each time step, t_n to t_{n+1}, the number of iterations k is controlled by the following error bound

$$\sum_i \sum_j |X_{j,i}^{k+1} - X_{j,i}^k|^2 / J_i < \mathrm{err}$$

where err is a preassigned small number and $X_{i,j}^k$ is the position vector on the jth grid point $s_i = j\Delta s$ on the ith filament at t_{n+1} after k iterations. When the above error bound is not satisfied after an assigned number of iterations (10 in our numerical code), the iteration procedure is repeated anew with the time step reduced by a factor of 2. If this reduction is required more than three times, the program is terminated. So far this has not occurred when the maximum CFL number is initially set at 0.5. To check the accuracy of the results, we compared test cases with grid number $J_i = 40$, 60, 80, 120, 160, 200, initial maximum CFL number = 0.5 and 0.25, and err = 10^{-6} and 10^{-7}. We found that a grid number of 60-80, a CFL of 0.5, and an err of 10^{-6} to be satisfactory in the sense that final positions of filaments before merging have accuracy of three significant figures. We use the larger number of grid points 80 when we expect that the self-merging is going to take place with the core size comparable to the local radius of curvature of the centerline. Since we are interested in the transient solutions, a small time incre-

ment Δt will be used to increase the accuracy and reduce the number of iterations for each time step. In the numerical examples to be mentioned in the next section, we choose the time step Δt with the initial maximum Courant-Friedrichs-Levy (CFL) number set at 0.25. In our numerical examples the iterations converge in less than five cycles with err equal to 10^{-6} until the merging is about to take place. The practical criteria for that instant when merging takes place will be specified in the next section. The computation based on the asymptotic theory will be terminated at that instant.

III. Numerical Results

A computational code for the equations of the matched asymptotic analysis described in Sec. II was developed to study the motion and interaction of vortex filaments. The code is being used to study systematically: 1) the effects of the initial core structure, which may not be similar, for a given initial shape $X(s,0)$, total strength Γ, and total axial flux M_0; 2) the effect of axial flow of various strength M_0 for given Γ, initial core structure, and shape $X(s,0)$; 3) the interaction of two filaments; and 4) the onset of various types of merging or interaction of filaments.

It was pointed out in Refs. 8-11 and emphasized in Ref. 23 that the asymptotic analysis was formulated under condition (4) that the effective core size $\delta(t)$ for a filament is much smaller than the other length scale in the flow. For flows induced by free vortex filaments in an unbounded domain, the other reference length scales are 1) the minimum radius of curvature $R_{\min}$ of a centerline C, 2) the minimum distance $d_{\min}$ between two "distinct" points on C, and 3) the minimum distance d_{ij} between two centerlines C_i and C_j. Condition (4) then implies

$$(R_{\min}/\delta)_i \geq k_i \gg 1, \text{ for } i=1,\ldots,N \tag{23a}$$

$$(d_{\min}/2\delta)_i \geq k_2 \gg 1, \text{ for } i=1,\ldots,N \tag{23b}$$

$$d_{ij}/(\delta_i+\delta_j) \geq k_3 \gg 1, \; i,j=1,\ldots,N \quad i\neq j \tag{23c}$$

Because of Eq. (23a), we define two "distinct" points on C by the condition that the arc length between them along C is finite, say, larger than $\pi\delta$. These three conditions (23a-23c) exclude self-merging, self-interaction, and intersection of two filaments, respectively. When there is background potential flow, say, flow around a body, additional conditions should be imposed so that the core structures will not overlap with the boundary layer along the body surface. The onset of merging is defined at the instant the equality sign holds in any of Eqs. (23a-23c). Noting that the vorticity in the merged region is of the order of $\exp(-k_\ell^2)$, $\ell=1,2,3$, we choose in our numerical examples $k_1=2$ and $k_2=k_3=1.5$. The extension of the asymptotic theory to moderate values of k_ℓ has also been justified by comparing the asymptotic solutions with the numerical solutions of the Navier-Stokes equations,[24,25] starting at an earlier instant with k_ℓ doubles. For each type of merging, the merged region can be "local" or "global," depending on whether condition (23a) or (23b) or (23c) is violated locally over an arc length much smaller than the entire length of the filament or is fulfilled globally over almost the entire length.

Figure 2 shows the three views of the centerline $X(s,t)$ of a single vortex filament at various instants from $t=0$ to the final instant $t=21.02$, when the effective core size becomes comparable to the minimum radius of curvature of the filament at $X=(0,1.9256,13.932)$.

The initial shape $X(s,0)$ of the centerline is an ellipse with the major axis equal to 2 along the x_1 axis and the minor axis equal to 1.5 along the x_2 axis. The physical data are $\nu=0.0045$, $\Gamma=5$, and hence $\epsilon=[\nu/\Gamma]^{1/2}=0.03$. At the initial instant, the core structure of the leading circumferential flow is a similarity solution with effective core size $\delta_0=(4\nu\tau_{20})^{1/2}=\sqrt{0.018}$, i.e., $\tau_{20}=1$. There is no large axial flow ($M_0=0$).

From Fig. 2 we see that the centerline ceases to be planar for $t>0$, due to the spacial variation of the radius of curvature. The centerline becomes almost planar at $t=4.75$, "the first half-period," with its shape nearly the same as the initial one with an interchange of the major and minor axes. At $t=12.30$, "the first period," the centerline once more becomes almost planar, with its shape nearly the same as the initial one. Due to the decay of the core structure, the motion becomes more aperiodic as the core size increases with t.

Let $x_1^*(t)$ and $x_2^*(t)$ denote the maximums of the x_1 and x_2 coordinates, respectively, of $X(s,t)$. Then the envelopes in the top view and the side view of $X(s,t)$ in Fig. 2 show the variations of $x_1^*(t)$ and $x_2^*(t)$, respectively.

Figure 3 illustrates the dependence of the "first period" of x_1^* on the Reynolds number $\Gamma/\nu=\epsilon^{-2}$ (on the initial core size for a given Γ) and the effect of large axial flow in the core. The initial shape of the centerline is the same as that in Fig. 2. Both the initial circumferential and axial velocity components are similarity solutions, with core size $\delta_0=2\sqrt{\nu}$, i.e., $\tau_{20}=1$. The figure shows that the movements of the filament slow down for larger ν/Γ, or larger initial core size. The axial flow in the core tends to slow down the movement, and the effect is more pronounced for larger ν/Γ.

Figure 4 demonstrates the effect of initial nonsimilar core structures. The initial shapes of the centerline of the filament and the physical constants are the same as those in Fig. 2. The envelope of the top view of $X(s,t)$ (the graph of $x_1^*(t)$ in Fig. 2) is reproduced as curve 1 Fig. 4. We recall that the core structure has a similar circumferential profile, with no axial flow and an initial effective core size δ_0. Curve 2 shows the corresponding graph of $x_1^*(t)$ for an initial nonsimilar vorticity profile with the shape of a top hat. The radius and the strength of the top-hat vorticity distribution are $\delta_T=\delta_0\sqrt{2}$ and $\Gamma/(\pi\delta_T^2)$, respectively. We note that the initial similarity

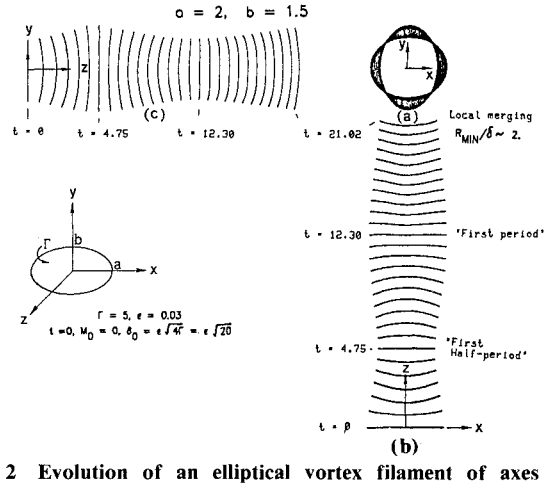

Fig. 2 Evolution of an elliptical vortex filament of axes ratio 1.5/2.0, $\Gamma=5$, $\epsilon=0.03$; a) plan view, b) side view, c) end view.

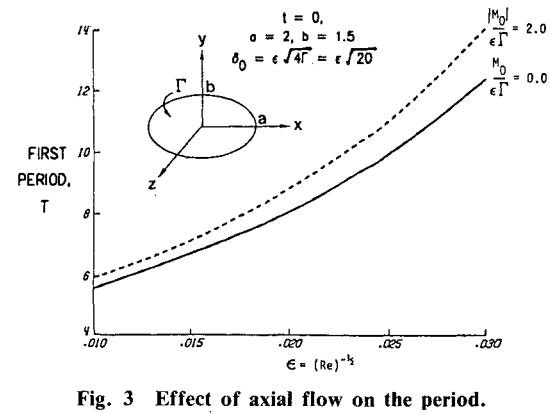

Fig. 3 Effect of axial flow on the period.

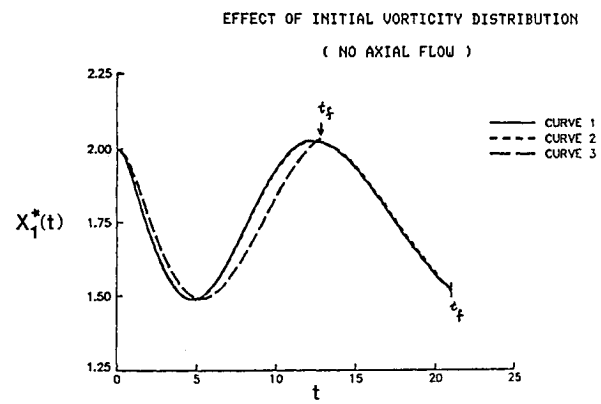

Fig. 4 Effect of initial nonsimilar core structures with $\Gamma=5$, $\epsilon=0.03$, and $M_0=0$.

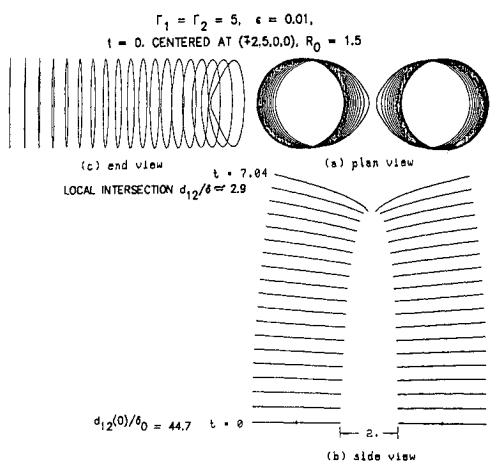

Fig. 5 Interaction of two filaments of the same strength $\Gamma_1=\Gamma_2=5$, $\epsilon=0.01$, $R_0=1.5$; centered at ∓ 2.50, 0, 0).

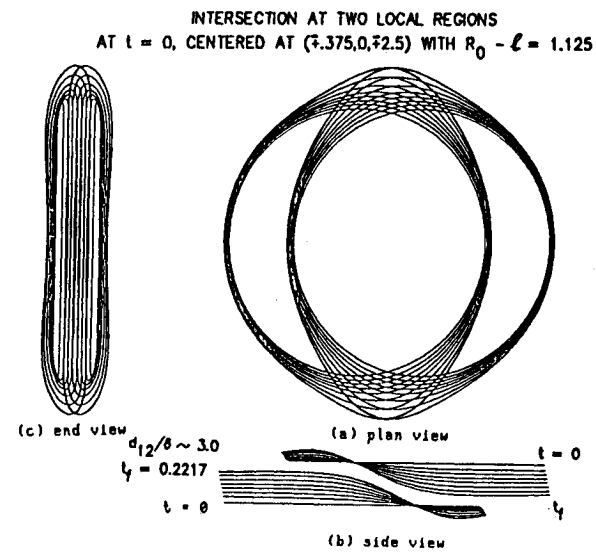

Fig. 6 Interaction of two filaments of equal but opposite strength $\Gamma_2=-\Gamma=5$, $R_0=1.5$; centered at (∓ 0.375, 0, ∓ 0.25).

profile for curve 1 and the top-hand distribution for curve 2 have not only the same total strength Γ but also the same second polar moment $\Gamma\delta_0^2$. The similarity solution is therefore the "optimum" approximation to the nonsimilar solution [see Eq. (20)]. We see that the difference between curves 1 and 2 is insignificant and that the predictions of the instant of local self-merging differ by only 0.51%.

Curve 3 in Fig. 4 shows the graph of $x_1^*(t)$ when the initial profile is that of a similarity solution of circulaton Γ, with a larger effective core radius $\delta_0\sqrt{2}$, which is the radius δ_T of the top-hat distribution for curve 2. The difference between curve 2 and 3 shows that the choice of core size for curve 3 is inferior to the "optimum" one for curve 1. The difference between curve 1 and curve 3 also demonstrates the effect of different initial core sizes. The core size for curve 3 is larger and the criterion for self-merging is satisfied near the end of the first period while curves 1 and 2 continue nearly a half-period longer. Additional calculations were made[16] for filaments with a large axial flow $\bar{w}_0\neq 0$. These numerical results demonstrate that, among all the similarity solutions, the one with an optimum initial core, which matches the total strength and the second polar moment of the nonsimilar initial profile, yields the best approximation of the nonsimilar solution. This fact was noted before in the two-dimensional and axisymmetric problems.[10,12]

Figures 5-8 show the interactions of two filaments with $\Gamma_1=|\Gamma_2|=5$, $\nu=0.0005$, and $\epsilon=0.01$. For their initial core structures, the circumferential flow in both filaments are the same, with the similarity solution with effective core size $\delta_0=(4\nu\tau_{20})^{1/2}=\sqrt{0.002}$, i.e., $\tau_{20}=1$. There is no large axial flow ($M_0=0$), and their centerlines are initially circles of the same radius, $R_0=1.5$.

Figure 5 shows the interaction of two filaments of the same strength $\Gamma_2=\Gamma_1$. It simulates two vortex rings created by two coplanar orifices facing the same direction. Initially ($t=0$), the rings lie in the x-y plane centered at ($\pm 2.5,0,0$). The minimum distance between them is 2, $d_{12}(0)=2=44.7\delta_0$. As t increases, the centerline of the rings become nonplanar and tilt toward each other. The shape of the rings deviates from a circle, and the deviation is more pronounced at the segments close to each other, where the effect of interaction is maximum. Figure 5 shows the three views of the centerline at different instants until $t_f=7.04$, with $\delta=1.25$ and $d_{12}=0.36<3\delta$. The two filaments touch each other according to condition (23c), and local merging takes place thereafter. Qualitatively similar results were obtained[22] for the same two filaments initially centered at ($\pm 2,0,0$). Since the initial minimum separation is halved and the mutual intereaction effect is larger, the instant of merging occurs sooner at $t_f=1.88$.

Figures 6-8 show the interactions of two filaments of equal but opposite strength $\Gamma_1=-\Gamma_2=5$. Initially ($t=0$), their centerline are circles with radius $R_0=1.5$. They lie in the plane $z\mp 0.25$ and are centered at ($\mp\ell$, 0, ∓ 0.25) with $\ell=0.375$, 1.30, and 1.375 for Figs. 6-8, respectively. These three figures illustrate three different types of interactions, namely, 1) intersection in two local regions, 2) touching, and 3) local self-merging. A fourth type is illustrated in Ref. 16 by a nearly head-on collision, when $0\leq\ell\ll 1$ and the merging takes place along the entire filament. Consequently, we have a global merging.

The initial distance between the centers of the two circles in 2ℓ, and their projections on the x-y plane overlap each other for $|x|<R_0-\ell$. We define $R_0-\ell$ as the initial overlap and call the filament on the left side the first filament. We use the polar angle θ for each circle as the parameter s for the centerline.

As ℓ increases, the initial overlap $R_0-\ell$ of the two centerlines decreases. Figure 6 shows the movements of the two filaments with $\ell=0.375$. They move toward each other with the "nonoverlapping" part of the centerline remaining nearly planar while the "overlapping" part bends backward. At $f_f=0.2217$, the core size δ is 0.04581, and the two filaments intersect at two local regions near the y-z plane with $\theta^*=\pm 75$ deg, and $d_{12}=0.1372\leq 3\delta$. The projection of the centerline on the x-y plane deviates from a circle, and the deviation is more pronounced near θ^*, where the interaction is the strongest.

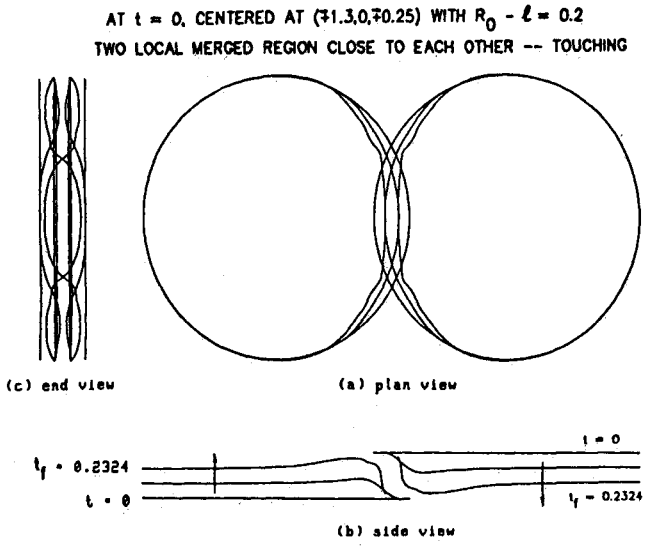

Fig. 7 Interaction of two filaments of equal but oppposite strength $\Gamma_2 = -\Gamma_1 = -5$, $R_0 = 1.5$; centered at $(\mp 1.30, 0, \mp 0.25)$.

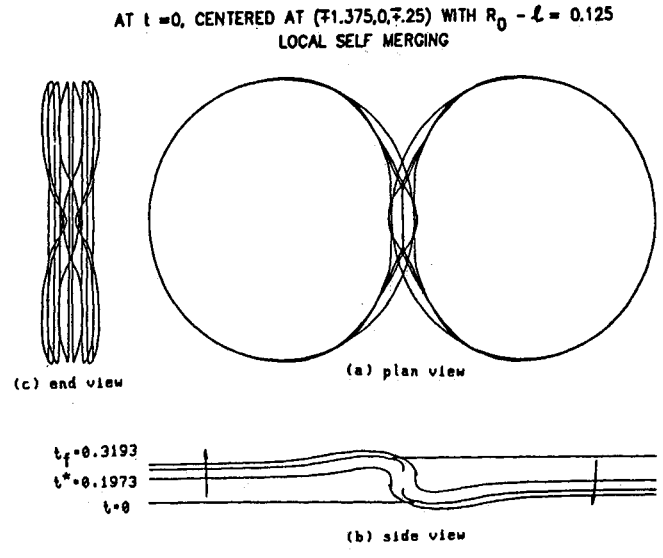

Fig. 8 Interaction of two filaments of equal but opposite strength $\Gamma_2 = -\Gamma_1 = -5$, $R_0 = 1.5$; centered at $(\mp 1.375, 0, \mp 0.25)$.

Figure 7 shows the movements of the two filaments with $\ell = \ell_c = 1.30$ and the initial overlap $R_0 - \ell = 0.2$. Qualitatively, the movements resemble those in Fig. 6, except that the overlapping portion is smaller and bends back more sharply. At $t_f = 0.2324$ the two filaments intersect at one local region near $\theta^* = 0$. They are in effect touching each other. We note that the time t_f of intersection decreases as ℓ increases from zero to ℓ_c while the initial overlap $R_0 - \ell$ decreases from 1.5 to 0.2.

For $\ell > \ell_c$ we expect the two filaments to pass each other without intersecting although their projections on the x-y plane do overlap initially. Figure 8 shows the movements of the two filaments with $\ell = 1.375$ and initial overlap $R_0 - \ell = 0.125$. We see from Fig. 8 that the two filaments move toward each other with the nonoverlapping portion retaining nearly the same circular shape while the small overlapping region bends backward sharply at almost a right angle to the x-y plane. When $t^* \sim 0.1973$, the two centerlines are nearly coplanar and the overlapping region bends backward sufficiently to allow the mutual passage of the two filaments. For $t > t^*$, the two filaments are moving away from each other and the effect of interaction is reversed. The portion that has bent backward sharply begins to stretch forward until local self-merging takes place at $t_f = 0.3193$.

As ℓ increases, the mutual interaction decreases and the local self-merging will take place at a later t_f. In the limit of $\ell \gg R_0$, there is no interaction between the two filaments. Each centerline moves forward and remains circular until the core size δ is no longer too small relative to R_0, and then total self-merging takes place. A numerical solution of the Navier-Stokes equations for a totally self-merged circular vortex ring was presented in Ref. 24.

IV. Classification of the Merging and Computational Domains for the Navier-Stokes Solutions

In the preceding section, we domonstrated the use of the asymptotic solutions to describe the motion and decay of slender vortex filaments until self-merging or merging of two filaments takes place. Criteria [Eqs. (23a-23c)] define the types of merging and the instant of their onset. After the onset, the evolution of the flowfield in a merged region requires, in general, a numerical solution of the Navier-Stokes equations in a bounded domain D. The initial data will be provided by the asymptotic solution. We have to specify the computational domain D containing the merged region and then formulate the appropriate conditions on the boundary ∂D. For this purpose, we classify the merged regions by their shapes and types of merging, whether the merging involves one or two filaments. Hence, we have only the following three types of merged regions:

1. Completely Merged in a Spherical Domain

This type includes global self-merging and/or self-intersection, i.e., Eq. (23a) and/or Eq. (23b) are violated for almost the entire filament. It also includes the global merging of two filaments when Eq. (23c) fails. Typical examples are the self-merging of a circular ring and head-on collision of two rings that are also in the stage of self-merging. Once the merging begins, the basic structure of the filament(s) will be lost forever. The numerical solution of the merging will be carried out in a spherical or cubical domain D containing the merged region. The size of D should be much larger than that of the merged region so that the flow is irrotational outside D.

Since the vorticity decays exponentially in distance from the center of the merged region, we impose the approximate boundary condition for the vorticity ω,

$$\omega = 0 \qquad \text{on the boundary } \partial D \tag{24}$$

The boundary conditions for the velocity V were formulated in Ref. 25. They were obtained by the expansion of the Poisson integral in terms of the moments of the vorticity distribution, using the integral invariants.[26] The computational code for this type of merging was developed, and several examples were presented in Refs. 27 and 28.

2. Totally Merged Filaments in a Slender Toroidal Domain

This type of merging may occur when the centerlines of the two slender filaments are nearly of the same shape in head-on collisions or in the catching up of one filament on the other. At the onset, the distance from any one point on one filament to the other becomes comparable to the core size. Condition (23c) breaks down along the entire length of the filaments while both filaments remain slender, fulfilling conditions (23a) and (23b). The numerical solution of the merging can be carried out in a slender toroidal domain D containing the merged filaments. The cross-sectional size of the domain S will be much larger than that of the merged region but much smaller than the mean radius of the torus.

We can again use Eq. (24) as the boundary condition for ω. The appropriate boundary conditions for V were

developed as Type 3 in Ref. 22 for axisymmetric problems. In general, we can develop the boundary conditions for V on the toroidal surface ∂D by an extending of the method in Ref. 24, that is, by expanding the Poisson integral in the toroidal coordinates (s,r,θ) since r/σ is large on ∂D where σ is the cross-sectional size of the merged region.

After a finite period of merging, the structure of a single slender filament or two distinct filaments may reappear. When this happens, the asymptotic analysis will be applicable thereafter.

3. Local Merging

We can have three kinds of local merging when Eq. (23a) or (23b) or (23c) is violated over only a small segment of the filament(s) much less than the length of the filament(s). The numerical solution of the merged region can be carried out in a spherical, cylindrical, or cubical domain D. Its size will be much larger than that of the merged vortical region but still much smaller than the size of the filament(s), for example, its length. Outside the domain D, the structures of two slender vortex filaments remain intact.

The vorticity outside D is not zero; therefore, a new formulation of the boundary conditions on ∂D for the vorticity ω and the velocity V are needed. A method was proposed in Ref. 22 that made use of the asymptotic solutions for the filaments ouside D. A numerical code implementing this method is being developed. We expect that after a finite period of merging, the structure of a single filament or two distinct filaments may reappear, and thereafter we can apply the asymptotic analysis.

V. Summary

A computational code is developed for the integro-differential equation governing the motion of the centerlines of slender vortex filaments submerged in a background potential flow. These equations, which were derived by the method asymptotic analysis, include the effects of the core structures (i.e., the large-magnitude circumferential and axial velocity components) having initial profiles, which may not be compatible with the similarity solutions. The analysis removes the singular parts of the Biot-Savart integral. Its contribution to the velocity of the centerline is given by its finite part, an integral of a piecewise continuous function. Numerical examples are presented that provide a study of the motion and decay of vortex filaments without boundaries. The initial configuration of the filaments are chosen to fulfill the basic assumption of the asymptotic analysis; that is, the effective core size is much smaller than other length scales in the flow [see Eq. (24)]. The numerical examples show that the addition of axial flow to the core structure tends to retard the motion of a filament and that its motion with an initial nonsimilar profile can be approximated by one with an optimum similarity profile. The latter has initial core size so chosen that its total strength and polar moment match those of the given initial profile. The computations are continued until the moment the aforementioned basic assumption [see Eq. (24)] is no longer valid and the merging or intersection of filaments begins. Various types of global or local merging or interaction are illustrated by numerical examples. They are classified as three types. For each type, the appropriate computational domain and boundary conditions are proposed so that numerical solution of the Navier-Stokes equation for the merged region can be carried out.

Acknowledgments

The research efforts of John Tavantzis and Lu Ting were partially supported by ONR Contract N000-14-80-C-0324 and by NASA Cooperative Agreement NCC1-58.

References

[1]Brown, C. W., "Aerodynamics of Wake Vortices," *AIAA Journal*, Vol. 11, April 1973, pp. 531-536.

[2]Van Dyke, M., *An Album of Fluid Motion*, Parabolic Press, Stanford, CA, 1982.

[3]Cornish, J. J., III, "Vortex Flow," Lockheed-Georgia Company, Marietta, GA, 1982.

[4]Donaldson, C. duP. and Bilanin, A. J., "Vortex Wakes of Conventional Aircarft," AGARD-AG-204, May 1975.

[5]Greene, G. C., "Wake Vortex Alleviation," AIAA Paper 81-0798, May 1981.

[6]*Aerodynamics of Vortical Type Flows in Three Dimensions*, AGARD-CP-342, 1983.

[7]Lamb, H., *Hydrodynamics*, Dover Publications, New York, 1949, pp. 202-246.

[8]Ting, L. and Tung, C., "Motion and Decay of a Vortex in a Non-Uniform Stream," *Physics of Fluids*, Vol. 8, 1965, pp. 1039-1051.

[9]Tung, C. and Ting, L., "Motion and Decay of a Vortex Ring," *Physics of Fluids*, Vol. 10, 1967, pp. 901-910.

[10]Ting, L., "Studies in the Motion and Decay of Vortices," *Aircraft and Wake Turbulence and Its Detection*, Plenum Press, New York, 1971, pp. 11-39.

[11]Callegari, A. and Ting, L., "Motion of a Curved Vortex Filament with Decaying Vortical Core and Axial Velocity," *SIAM Journal of Applied Mathematics*, Vol. 35, No. 1, July 1978, pp. 148-175.

[12]Chorin, A. J. and Marsden, J. E., *A Mathematical Introduction to Fluid Dynamics*, Springer-Verlag, New York, 1979.

[13]Ashurst, W. T., "Numerical Simulations of Turbulent Mixing Layers via Vortex Dynamics," *Turbulent Shear Flows I*, edited by F. Durst, B. E. Lander, F. W. Schmidt, and J. H. Whitelan, Springer-Verlag, New York, 1979, pp. 402-413.

[14]Zabusky, N. J., "Computational Synergetics and Mathematical Innovation," *Journal of Computational Physics*, Vol. 43, No. 2, Oct. 1981, pp. 195-249.

[15]Chorin, A. J., "The Evolution of a Turbulent Vortex," *Communications in Mathematical Physics*, Vol. 83, No. 4, March 1982, pp. 517-535.

[16]Beale, T. B. and Majda, A., "Vortex Methods I, II," *Mathematics of Computation*, Vol. 39, No. 159, July 1982, pp. 1-27, 29-52.

[17]Anderson, C. and Greengard, C., "On Vortex Methods," *SIAM Journal of Numerical Analysis*, Vol. 22, No. 3, June 1985, pp. 413-440.

[18]Siggia, E. D., "Collapse and Amplification of a Vortex Filament," *Physics of Fluids*, Vol. 28, March 1985, pp. 794-805.

[19]Saffman, P. G., "The Velocity of Viscous Vortex Rings," *Studies in Applied Mathematics*, Vol. 49, 1970, pp. 371-380.

[20]Moore, D. W. and Saffman, P. G., "The Motion of a Vortex Filament with Axial Flow," *Philosophical Transactions of the Royal Society*, London, Ser. A 272, 1972, pp. 403-429.

[21]Leonard, A., "Numerical Simulation of Interacting Three-Dimensional Vortex Filaments," *Lecture Notes in Physics*, Vol. 35, Springer-Verlag, New York, 1974, pp. 245-250.

[22]Liu, C. H., Tavantzis, J., and Ting, L., "Numerical Studies of Motion of Vortex Filaments—Implementing the Asymptotic Analysis," AIAA Paper 84-1542, June 1984.

[23]Ting, L., "Studies on the Motion and Decay of Vortex Filaments," *Advances in Fluid Mechanics*, Vol. 148, edited by E. Krause, Springer-Verlag, New York, 1981, pp. 67-105.

[24]Liu, C. H. and Ting, L., "Numerical Solution of Viscous Flow in Unbounded Fluid," *Lecture Notes in Physics*, Vol. 170, Springer-Verlag, New York, 1982, pp. 357-363.

[25]Ting, L., "On the Application of the Integral Invariants and Decay Laws of Vorticity Distributions," *Journal of Fluid Mechanics*, Vol. 127, Feb. 1983, pp. 497-506.

[26]Howard, L. N., "Divergence Formulas Involving Vorticity," *Archive for Rational Mechanics and Analysis*, Vol. 1, No. 1, 1957, pp. 113-123.

[27]Chamberlain, J. P. and Liu, C. H., "Navier-Stokes Calculations for Unsteady Three-Dimensional Vortical Flows in Unbounded Domains," *AIAA Journal*, Vol. 23, June 1985, pp. 868-874.

[28]Chamberlain, J. P. and Weston, R. P., "Three-Dimensional Navier-Stokes Calculations of Multiple Interacting Vortex Rings," AIAA Paper 84-1545, June 1984.